

Article

Photocatalytic Degradation of Organic Dye under UV-A Irradiation Using TiO₂-Vetiver Multifunctional Nano Particles

Le Thi Song Thao ^{1,2}, Trinh Trung Tri Dang ^{1,2}, Wilawan Khanitchaidecha ^{1,2}, Duangdao Channei ^{3,4} and Auppatham Nakaruk ^{5,*}

¹ Department of Civil Engineering, Faculty of Engineering, Naresuan University, Phitsanulok 65000, Thailand; janetle.176@gmail.com (L.T.S.T.); ttttdang247@gmail.com (T.T.T.D.); wilawank1@gmail.com (W.K.)

² Centre of Excellence for Innovation and Technology for Water Treatment, Naresuan University, Phitsanulok 65000, Thailand

³ Department of Chemistry, Faculty of Science, Naresuan University, Phitsanulok 65000, Thailand; duangdaoc@nu.ac.th

⁴ Research Center for Academic Excellence in Petroleum, Petrochemicals and Advanced Materials, Naresuan University, Phitsanulok 65000, Thailand

⁵ Department of Industrial Engineering, Faculty of Engineering, Naresuan University, Phitsanulok 65000, Thailand; auppathamn@nu.ac.th

* Correspondence: auppathamn@nu.ac.th; Tel.: +66-5596-4224

Academic Editor: Walid Daoud

Received: 29 November 2016; Accepted: 25 January 2017; Published: 30 January 2017

Abstract: The properties and photocatalytic performance of anatase nanoparticles of pure TiO₂ and a core-shell structure of TiO₂ on calcined vetiver grass leaves have been compared. Samples were fabricated by sol-gel and heating at 450 °C for 5 h. The comparison was based on data for X-ray diffraction (XRD), UV-Vis spectrophotometry, photoluminescence, transmission electron microscopy, specific surface area measurement, pore volume assessment, and methylene blue degradation testing. The results showed that the pure TiO₂ consisted of agglomerated equiaxed nanoparticles of individual grain sizes in the range 10–20 nm. In contrast, the TiO₂-vetiver composite exhibited a core-shell structure consisting of a carbonaceous core and TiO₂ shell of thickness 10–15 nm. These features influenced the photocatalytic performance in such a way that the lower cross-sectional area, greater surface area, and higher pore volume of the TiO₂ shell increased the number of active sites, reduced the charge carrier diffusion distance, and reduced the recombination rate, thereby improving the photocatalytic activity. This improvement derived from morphological characteristics rather than crystallographic, semiconducting, or optical properties. The improved performance of the TiO₂-vetiver core-shell was unexpected since the X-ray diffraction data showed that the crystallinity of the TiO₂ was lower than that of the pure TiO₂. These outcomes are attributed to the reducing effect of the carbon on the TiO₂ during heating, thereby facilitating the formation of oxygen vacancies, which enhance charge separation and hence photocatalysis by TiO₂.

Keywords: TiO₂; vetiver grass; core-shell; photocatalysis; carbon reduction; nanostructure

1. Introduction

Water is an indispensable part of life because it is essential for various purposes, including drinking, public hygiene, energy, agriculture, and industry. However, freshwater resources currently are diminishing due to the increasing growth of global population, over-exploitation, and water pollution [1]. In order to deal with water scarcity, wastewater treatment and reclamation are

favourable approaches because they can prevent water pollution, protect public health, and provide reclaimed water source for agriculture and industry [2].

The textile industries annually produce huge amounts of wastewater that contains organic dyes, which significantly contribute to global water pollution [3]. Most synthetic dyes used in the textile industries consist of aromatic ring structures, which make them toxic, chemically resistant, and non-biodegradable in the natural environment [4,5]. Therefore, removal of organic dyes is an important target in wastewater treatment and reclamation.

The key criterion in wastewater treatment and reclamation is the quality of the treated water so that it can be determined as safe for use. At present, some common technologies used in wastewater treatment include sedimentation, flocculation and coagulation, filtration, adsorption, and biological processes. These traditional wastewater treatment technologies have had a long history in large-scale applications and effectiveness for the removal of various pollutants, such as organic compounds, nutrients, pathogens, and heavy metals [6]. However, a significant drawback of these technologies is the generation of secondary waste, which requires additional post-treatment.

In order to overcome secondary waste generation from wastewater treatment and satisfy the stringent standards for water treatment and use, technologies based on photocatalysis have attracted considerable interest. Among the semiconductor photocatalysts, TiO_2 is used widely owing to its high photoactivity, photocorrosion resistance, thermal stability, non-toxicity, cost effectiveness, and potential applications under UV light (300–390 nm) [7,8]. When excited by a light source of energy equal to or greater than the band gap of the TiO_2 photocatalyst (3.0–3.2 eV [9]), electron and hole pairs are generated. The generated holes then can transfer to the surface of TiO_2 particles and react with water to form hydroxyl radicals ($\bullet\text{OH}$) and superoxide radicals ($\bullet\text{O}_2^-$) [10]. These radicals then act as or react with the environment to produce reactive oxygen species (ROS) in the form of hydroxyl ($\bullet\text{OH}$) groups, hyperperoxyl ($\bullet\text{HO}_2$) groups, and hydrogen peroxide (H_2O_2). These ROS have the advantage of being able to mineralise a wide range of organic compounds in wastewater into simpler organic products [11] or to decompose them completely into carbon dioxide and weak mineral acids [12–14].

The effectiveness of pollutant removal can be increased through the applications of the (1) surface modification [15–17]; (2) band gap narrowing [18–20]; and (3) co-mechanisms of adsorption by adsorbent and photocatalysis [21]. Consequently, there are many studies that have reported the immobilisation of TiO_2 particles on adsorbents such as zeolites, activated carbon, silica, and clays [22–26]. Furthermore, the immobilisation of TiO_2 on an adsorbent can help to reduce the wash-out of TiO_2 into the treatment system [27].

Zeolites and activated carbon are two of the most commonly used adsorbents in wastewater treatment. Both can be synthesised from agricultural wastes, such as coconut shell, straw, rice husk, bamboo, sedge weed, pokeweed, and sugarcane bagasse; these approaches are attractive from the perspectives of cost effectiveness and reduction of waste generation [28,29]. Amongst agricultural wastes, vetiver grass (*Vetiveria zizanioides* (L.) Nash) is a potential precursor, as it is most frequently used for erosion control and oil extraction in many tropical and subtropical countries [30]. The fragrant and volatile oil extracted from the roots of vetiver grass is used commercially in a range of industries, including perfumery, cosmetics, soap, and pharmaceuticals [31]. In environmental applications, vetiver grass has shown an ability to accumulate persistent organic pollutants (POPs), polycyclic aromatic hydrocarbons (PAHs), phenol, and a variety of heavy metals from contaminated soil and water [31–33]. However, the principal uses of vetiver grass for erosion control and extracted oil production result in the production of a large amount of agricultural waste in the form of its unused leaves [34].

In the present work, vetiver leaves were used as a precursor to synthesise a multifunctional material combining the adsorption ability of the vetiver leaves and the photocatalytic activity of TiO_2 . The synthesised material was characterised for a range of physicochemical properties and its applicability to wastewater treatment assessed by degradation of the organic dye methylene blue (MB). 2. Methodology.

2.1. Preparation of Vetiver Adsorbent

Vetiver grass was collected from the field in Phitsanulok Province, Thailand. Only the leaves of the vetiver grass were used to synthesise the adsorbent while other parts were removed. After cleaning with water to remove dirt, the vetiver leaves were dried in a muffle furnace at 105 °C for 12 h in order to remove moisture. The dried vetiver leaves were crushed with a porcelain mortar and pestle and sieved to a particle size in the range 0.1–0.6 mm, after which they were pyrolysed in the same muffle furnace at 600 °C for 3 h, followed by natural cooling. After pyrolysis, the residue was stored in an airtight container. The main inorganic components of the solid residue of vetiver leaves were determined previously to be potassium (45 wt%) and silicon (27 wt%) [35]. The physical and chemical properties of dried vetiver and adsorption mechanism were reported in the previous work [35].

2.2. Synthesis of Pure TiO₂ and TiO₂-Vetiver Core–Shell

The pure TiO₂ and TiO₂-vetiver core–shell was synthesised using a sol-gel method reported elsewhere [36]. For the latter, 1 g of calcined vetiver adsorbent was added to a mixture of 12.5 mL of titanium isopropoxide (TTIP), 80 mL of 2-propanol, and 3 mL of deionised (DI) water, after which blending was achieved by magnetic stirring for 4 h. The resultant suspension was filtered, washed by double distilled water, and dried at 105 °C for 12 h. The dried product then was calcined in the muffle furnace at 450 °C for 5 h in (3 °C/min) order to recrystallise the TiO₂, followed by natural cooling. After calcination, the residue was stored in an airtight container. Pure TiO₂ was prepared by the same procedure but without the addition of calcined vetiver.

2.3. Characterisation

For both pure TiO₂ and the TiO₂-vetiver core–shell, the following characterisation was undertaken. The mineralogies were determined by X-ray diffraction (XRD, Philips X' Pert PRO PW 3719). The crystallite size of particle was calculated using the Scherrer's equation [37]. The band gaps were calculated from data obtained by UV-Vis spectrophotometry from the diffuse reflectance spectra (DRS, Shimadzu UV-3600) with an integrating sphere attachment (Shimadzu ISR-3100) and the application of the Kubelka–Munk equation [38]. Photoluminescence spectra (PL) were recorded at 300 nm at room temperature a using spectrophotometer (Horiba Jobin Yvon Fluoromax-4). The morphologies were assessed by transmission electron microscopy (TEM, JEOL JSM-2010). The specific surface areas and pore size distributions were determined by N₂ gas adsorption-desorption using the Brunauer–Emmett–Teller (BET) method (Quantachrome Adtosorb 1 MP).

2.4. Photocatalytic Performance Testing

Methylene blue (MB, Sigma-Aldrich (Singapore), ≥95%) was used as the organic dye pollutant. A typical batch test involved mixing 0.01 g of the synthesised core–shell or pure TiO₂ with 50 mL of MB aqueous solution of 10⁻⁵ M concentration and magnetic stirring for 12 h in dark conditions (without UV-A irradiation) in order to adsorb the MB maximally on the particle surfaces. The suspensions then were irradiated by UV-A (two 20 W black lights, 370 nm) for 4 h. The irradiation was from above and the distance to the suspension surface was 15 cm. At periodic intervals of irradiation, a small sample of liquid was removed using a vacuum filter. The removed aliquot then was characterised by UV-Vis spectrophotometry using the standard absorbance intensity of $\lambda_{\max} = 664$ nm using the UV-visible spectrophotometer.

3. Results and Discussion

Figure 1 shows the XRD patterns for pure TiO₂ and the TiO₂-vetiver core–shell. The sharp peaks at 25.2°, 37.6°, 48.0°, 54.9°, 62.6°, 70.3°, and 75.0° 2 θ for pure TiO₂ show that it consists solely of the anatase polymorph [39]. In contrast, the TiO₂-vetiver core–shell peaks also indicate anatase but of lower intensities, which are attributed to the effect of the amorphous residue of the vetiver grass leaves. The reduced intensities, which derived from reduced crystallinity of the anatase, probably

resulted from the one or more of the following causes. First, silicon is known as a grain growth inhibitor for TiO_2 [40], which may have had a similar effect in suppressing nucleation and hence growth. Second, the crystal radii of K and Si in sixfold coordination (0.152 nm and 0.054 nm, respectively) are considerably different from that of Ti (0.0745 nm) [41] and the interstitial site (0.0782 nm) [42]. Consequently, if these dissolved in the TiO_2 lattice, they would have served to destabilise it. Third, carbon is a very strong reducing agent, so the Ti^{4+} (0.0745 nm) could have been reduced partially to Ti^{3+} (0.081 nm) [41], which could have expanded the lattice at these sites and contracted the lattice at the sites of the charge-compensating oxygen vacancies, which also would have had the potential to destabilise the lattice.

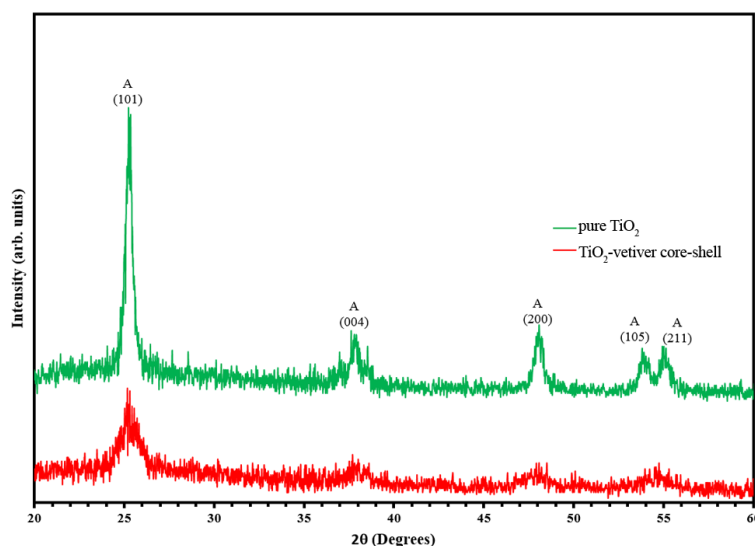


Figure 1. XRD patterns of pure TiO_2 and TiO_2 -vetiver core-shell.

The data used to calculate the optical indirect band gaps, which are shown in Figure 2, indicate that these are 3.58 eV and 3.66 eV for pure TiO_2 and the TiO_2 -vetiver core-shell, respectively. The band gap of the former was higher than the commonly reported value of 3.2 eV [9]. However, the band gap of anatase TiO_2 has been reported to cover a wide range of 3.23–3.59 eV [39]. Although the determined value is within this range, it is possible that it reflects silicon contamination, which is known to increase the band gap [9,43]. The even higher band gap of the TiO_2 -vetiver core-shell is likely to derive from the previously mentioned effect of carbon in the partial reduction of TiO_2 . Consequently, the XRD and band gap data are mutually supportive in suggesting that the presence of carbon caused lattice destabilisation and partial amorphisation. This is supported by modeling of the band gaps of both reduced TiO_2 , which contains oxygen vacancies [44] and of amorphous TiO_2 [45], which were substantially higher than that of the stoichiometric crystalline analogue.

Figure 3 shows photoluminescence (PL) spectra of pure TiO_2 and the TiO_2 -vetiver core-shell. Since PL emission occurs upon the recombination of the photogenerated electrons and holes [46], then the higher PL intensity of pure TiO_2 and that of the TiO_2 -vetiver core-shell suggests that the latter experienced enhanced charge separation and so exhibited a reduced recombination rate [47,48]. These effects would increase the probability for electrons and holes to form ROS and hence increase the photocatalytic activity [36,48].

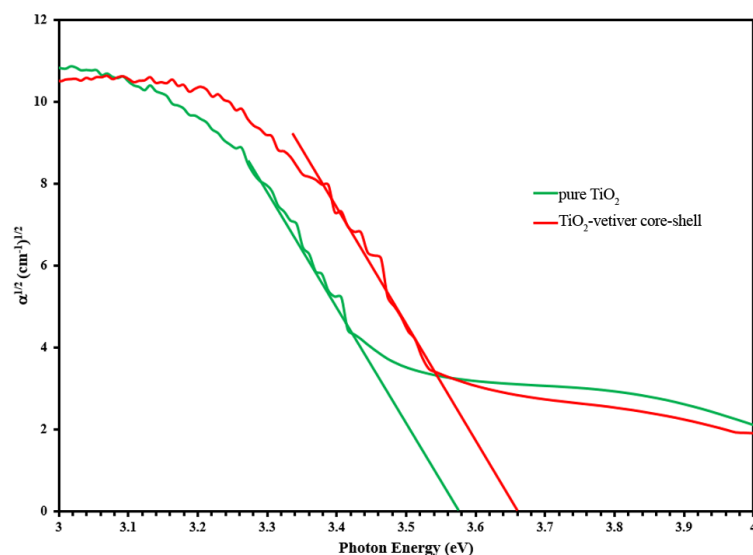


Figure 2. Optical indirect band gaps calculated from DRS data for pure TiO₂ and TiO₂-vetiver core-shell.

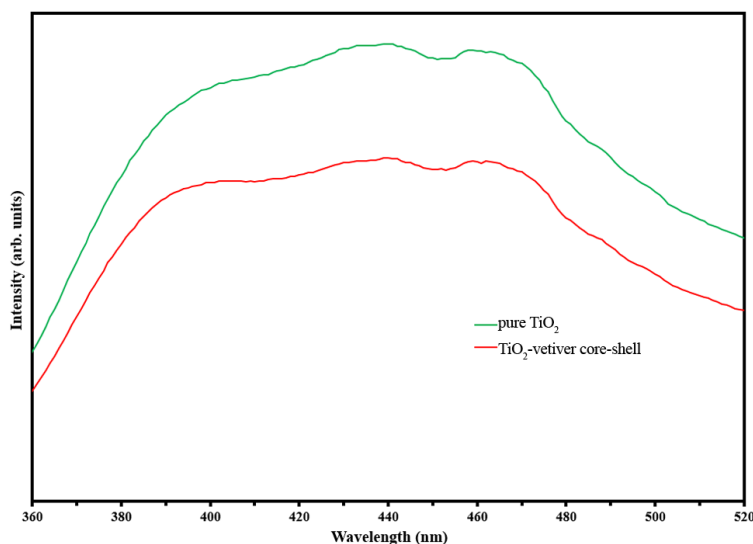


Figure 3. Photoluminescence (PL) spectra of pure TiO₂ and TiO₂-vetiver core-shell.

For the TiO₂-vetiver core-shell, it is likely that reduction by carbon and the consequent generation of oxygen vacancies are responsible for this since it has been reported that oxygen vacancies can enhance charge separation by acting as electron donors [49,50]. It is unlikely that dissolved K or Si played a role since (1) it is highly unlikely that K would dissolve either substitutionally or interstitially owing to size considerations; (2) Si dissolved substitutionally would not affect ionic charge compensation and hence create no oxygen vacancies; and (3) Si dissolved interstitially is likely to have resulted in ionic charge compensation by the formation of Ti vacancies. While Ti vacancies could have acted as hole donors, it is considered that the displacement of Ti⁴⁺ by Si⁴⁺ and the resultant formation of Ti vacancies are energetically unfavorable. It has to be noted that, in this work, the increasing of oxygen vacancy has not been directly observed. The increase of oxygen vacancy is implied from the increasing of surface area, which can lead to increasing the surface defects and oxygen vacancy [51–53].

Figure 4 shows TEM images of pure TiO₂ and the TiO₂-vetiver core-shell. The pure TiO₂ was equiaxed and of particle size in the range 10–20 nm, albeit highly agglomerated. It has to be noted that the particle size is very close to the crystallite size, as shown in Table 1. It can be said that the

pure TiO₂ is single grain particle. More interestingly, the TiO₂-vetiver core-shell exhibited a core-shell structure, where the vetiver acted as the core and the TiO₂ acted as the shell. The size of the TiO₂-vetiver core-shell was variable, depending on the nature of the vetiver substrate. The TiO₂ shell was continuous and of thickness in the range 10–15 nm.

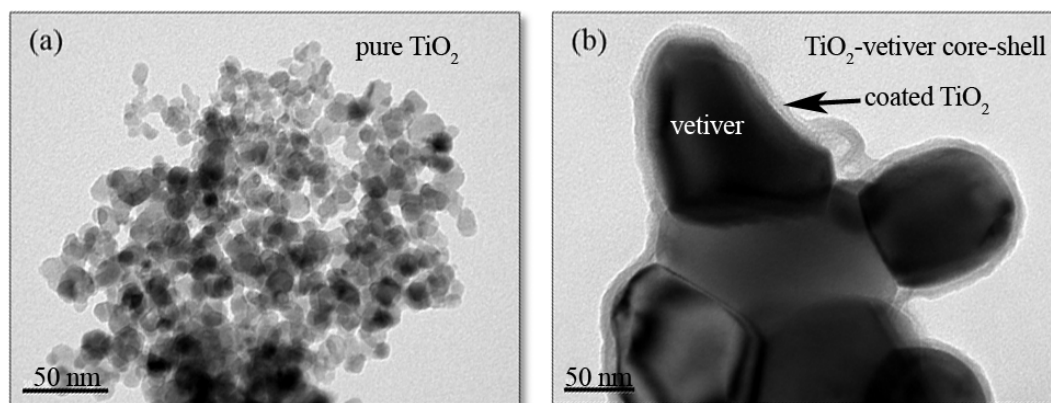


Figure 4. TEM images of (a) pure TiO₂; and (b) TiO₂-vetiver core-shell.

Such core-shell structures have gained considerable interest owing to their ability to enhance both charge separation and resistance to photocorrosion. Analogues of the present core-shell structure exist in the form of TiO₂ on the surfaces of carbon nanotubes (CNT) [54], TiO₂ coated on amorphous carbon [55], and the converse arrangement of a TiO₂ core and graphitic carbon shell [56].

N₂ adsorption-desorption isotherms of the pure TiO₂ and TiO₂-vetiver core-shell were also studied, as shown in Figure 5. The gas-adsorption isotherm is reported as the volume of gas adsorbed as a function of P/P₀. The results suggest that the prepared samples own typical Type IV isotherm. The gap between equilibrium adsorption and desorption pressures above P/P₀ of about 0.4, further confirming the characteristic of the mesoporous material.

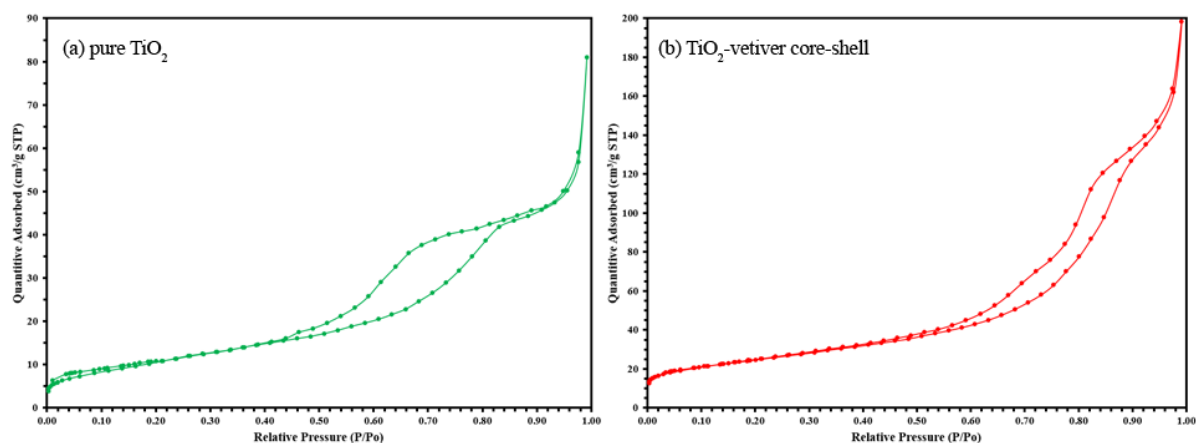


Figure 5. Nitrogen adsorption-desorption isotherm plots for (a) pure TiO₂; and (b) TiO₂-vetiver core-shell.

The results for the specific surface area and pore volume of pure TiO₂ and the TiO₂-vetiver core-shell are given in Table 1. It can be seen that the values for the pure TiO₂ are less than half those of the TiO₂-vetiver core-shell. The evidence for the reason for these differences lies in the nature of the TiO₂ shell of the TiO₂-vetiver core-shell. While the pure TiO₂ appears to have a considerably greater specific surface area, even with the agglomeration, as well as greater pore volume, the TiO₂ shell of the TiO₂-vetiver core-shell appears to be smooth. This apparent contradiction can be explained by closer examination of the TiO₂ shell, which reveals a granular nanostructure that exhibits both surface

topography and a network of spherical pores in the sub-nanometre size range. The unexpected presence of the pores is likely to have resulted from the oxidation of the carbon during annealing, which would have disturbed the establishment of the solid nanostructure upon recrystallisation of the TiO₂. Since the pores appear to be spherical, this suggests gas entrapment during the process. It also is possible that the pores were ruptured and hence continuous, which would increase the specific surface area further.

Figure 6a shows the complete data for MB adsorption followed by MB degradation. These data confirm that the pure TiO₂ has less than half the surface area of the TiO₂-vetiver core-shell. Figure 6b shows the normalised data for MB degradation, where it can be seen that the extent of MB degradation by the TiO₂-vetiver core-shell effectively was complete within 2 h. The pure TiO₂ appears to have experienced a 1 h time lag, after which the kinetics of MB degradation were similar to those of the TiO₂-vetiver core-shell, although the process does not appear to have reached steady-state after 4 h. It is clear that both photocatalyst types perform considerably better under UV-A light.

The preceding data suggest that the photocatalytic activity of the pure TiO₂ is somewhat inferior to that of the TiO₂-vetiver core-shell. This observation is consistent with the findings for the photoluminescence (Figure 3) and specific surface area data (Table 1), but it contradicts the data for the X-ray diffraction (Figure 1) and the band gap (Figure 2). From this, it is concluded that the controlling factors in the performance depend more on a reduced recombination rate (photoluminescence) and the number of surface active sites (specific surface area) rather than the crystallinity (X-ray diffraction) or the semiconducting and optical properties (band gap). In addition, the charge carrier diffusion distance in the TiO₂-vetiver core-shell would be relatively short owing to the 10–15 nm shell thickness and the possibility that it could be even less owing to the thinner walls resulting from the porosity. The diffusion distance in the pure TiO₂ would be longer owing to the larger 10–20 nm (solid) grain size. It is well known that the recombination rate decreases with decreasing charge carrier diffusion distance. Figure 7 shows the kinetic rate of MB removal. It can be seen that after irradiation the MB was completely removed in 2 h by TiO₂-vetiver core-shell. Since the TiO₂-vetiver core-shell has higher surface area and volume of pores, then this can result higher adsorption (Figure 6a). Then, during the photocatalytic mechanism (after irradiation), the MB at the surface could be decomposed quickly so the surface can adsorb more MB. It can be said that the co-mechanisms of adsorption by adsorbent and photocatalysis lead to higher performance compared to only photocatalytic of pure TiO₂.

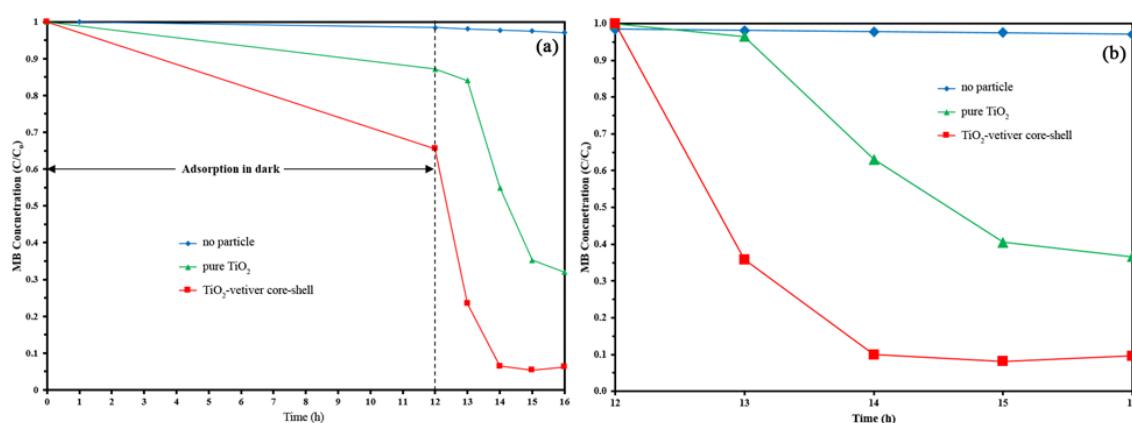


Figure 6. Photocatalytic activity of pure TiO₂ and TiO₂-vetiver core-shells, showing (a) data for complete test sequence; and (b) data normalised following MB adsorption.

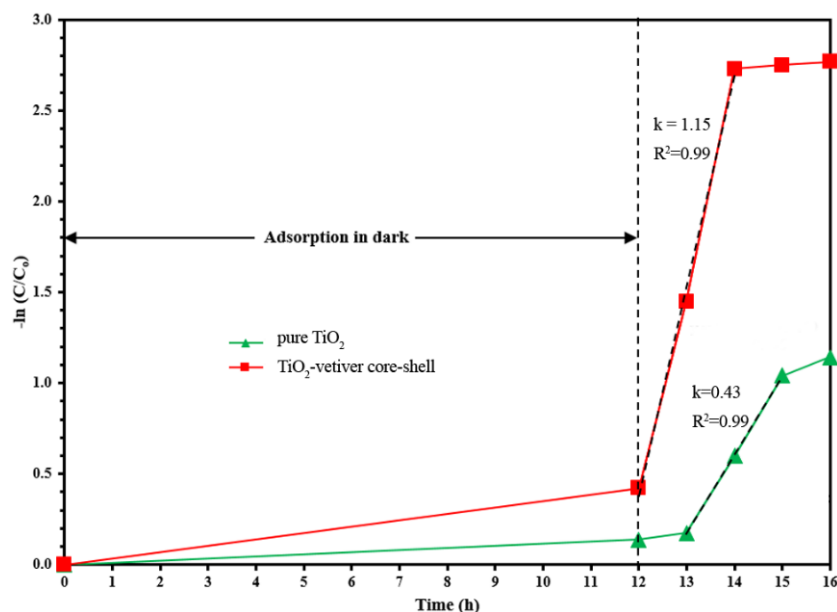


Figure 7. The kinetic of methylene blue degradation.

Data provides the surface area-normalised degradation constants. The comparison of normalised degradation constants excluded the influence of surface areas. In order to investigate the effect of surface area from the adsorbent on the degradation activity of TiO₂, the surface area-normalised degradation values against light irradiation time were plotted as shown in Figure 8 and the calculated surface area-normalised rate constants are presented in Table 1. The results clearly suggested that surface area of the catalyst has a crucial impact on the activity of degradation in this study because the surface area-normalised rate constants of TiO₂-vetiver core-shell are increased from the pure TiO₂.

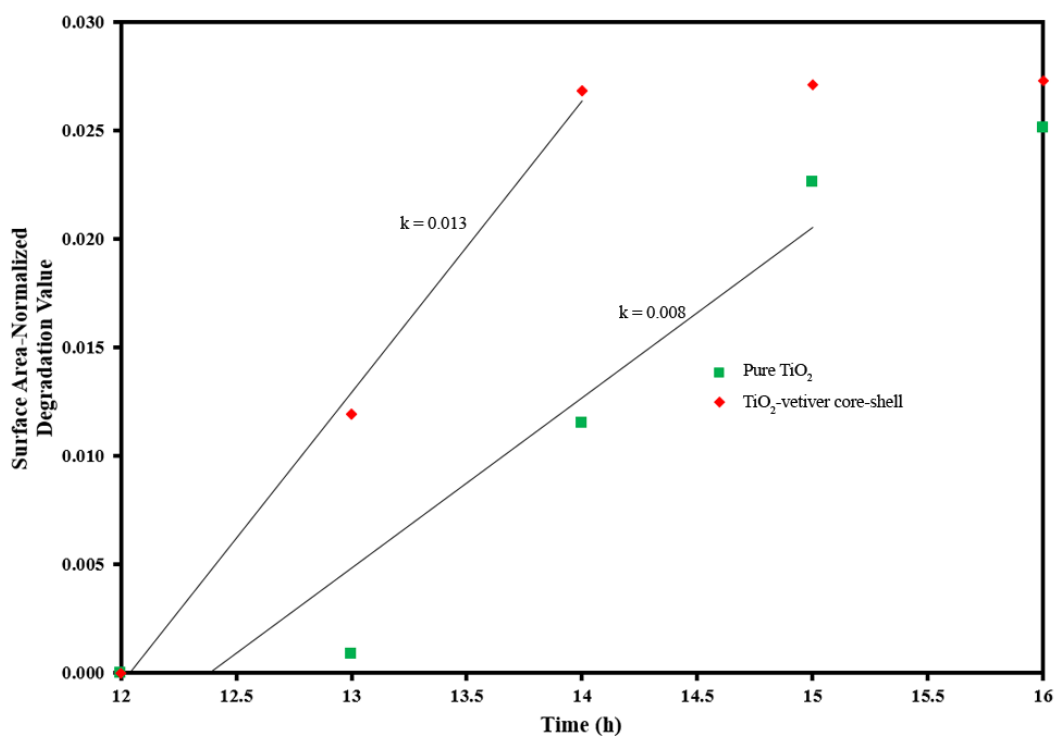


Figure 8. Kinetics plots of the surface area-normalised degradation values against light irradiation time.

The schematic representation of the photocatalytic mechanism is present in Figure 9. It can be explained that during the adsorption process MB can be adsorbed at the surface of TiO₂-vetiver core-shell as can be seen in Figure 5a. After irradiation, the photocatalytic at the surface of TiO₂-vetiver core-shell can occur immediately. This results in enhancing the photocatalytic performance of MB degradation.

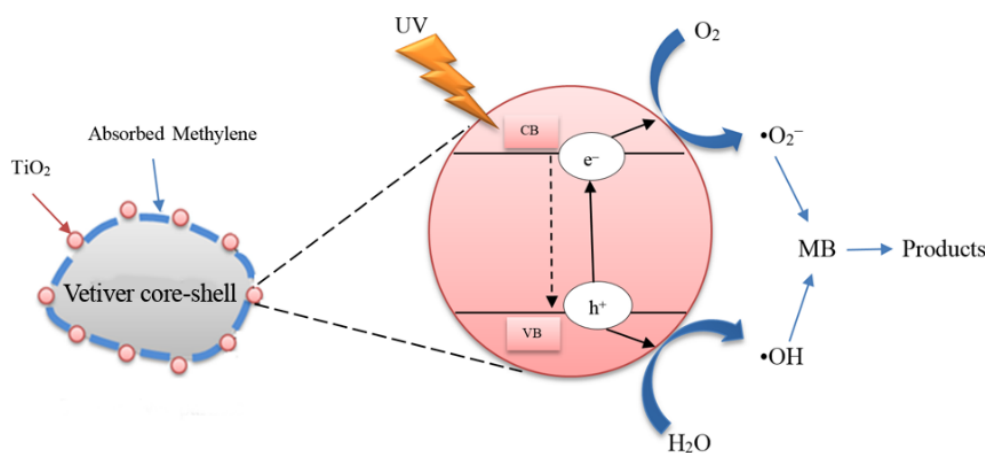


Figure 9. The schematic representation of the photocatalytic mechanism.

Table 1. BET data for surface properties of pure TiO₂ and TiO₂-vetiver core-shell.

Sample	Specific Surface Area (m ² /g)	Pore Volume (cm ³ /g)	Crystallite Size at (101) nm	Surface Area-Normalised Rate Constants (h ⁻¹ ·m ⁻² ·g)
Pure TiO ₂	40	0.1252	21	0.008
TiO ₂ -Vetiver Core-shell	86	0.3065	14	0.013

4. Conclusions

The present work reports a comparison between nanoparticles of pure TiO₂ and a core-shell structure of TiO₂ on calcined vetiver grass leaves. The samples were fabricated using a sol-gel method that involved heating at 450 °C for 5 h, which yielded the anatase polymorph of TiO₂. The comparison was based on data for X-ray diffraction, UV-Vis spectrophotometry, photoluminescence, transmission electron microscopy, specific surface area measurement, pore volume assessment, and methylene blue degradation testing.

The results showed that the pure TiO₂ consisted of agglomerated equiaxed nanoparticles of individual grain sizes in the range 10–20 nm. In contrast, the TiO₂-vetiver composite exhibited a core-shell structure consisting of a carbonaceous core and TiO₂ shell of thickness 10–15 nm. The TiO₂ shell formed a continuous coating with topography and porous network at a sub-nanometre scale. These features appear to have had a significant influence on the photocatalytic performance in that, compared to the pure TiO₂, the lower cross-sectional area, greater surface area, and higher pore volume of the TiO₂ shell potentially increased the number of active sites, reduced the charge carrier diffusion distance, and reduced the recombination rate, thereby improving the photocatalytic activity. This improvement derived from morphological characteristics rather than crystallographic, semiconducting, or optical properties.

The improved performance of the TiO₂-vetiver core-shell was unexpected in light of the X-ray diffraction data, which showed that the crystallinity of the TiO₂ was lower than that of the pure TiO₂. It also was unexpected in consideration of the unusually high band gap of the TiO₂ shell. However, both of these outcomes are likely to have been generated through the reducing effect of the carbon on the TiO₂ during heating, thereby facilitating the formation of oxygen vacancies, which enhance charge separation and hence photocatalysis by TiO₂. In this sense, the effect of charge separation dominated those of crystallinity and band gap. It has to be noted that, in this work, the increasing of

oxygen vacancy has not been directly observed. The increase of oxygen vacancy is implied from the increasing of surface area, which can lead to increasing the surface defects and oxygen vacancy.

Acknowledgments: The authors would like to thank Naresuan University for the financial support, which enabled this research.

Author Contributions: W.K. and A.N. conceived and designed the experiments and analyses; L.T.S.T. and T.T.T.D. performed the experiments; D.C. undertook the calculations; L.T.S.T., W.K., D.C. and A.N. analyzed the data; L.T.S.T. wrote the initial draft of the paper; A.N. wrote the final draft of the paper.

Conflicts of Interest: The authors declare no conflict of interest.

References

1. *Managing Water Uncertainty and Risk*; The United Nations World Water Development Report 4; 2012; Volume 1. Available online: <http://www.unesco.org/new/en/natural-sciences/environment/water/wwap/wwdr/wwdr4-2012/> (accessed on 1 November 2016)
2. Vo, P.T.; Ngo, H.H.; Guo, W.; Zhou, J.L.; Nguyen, P.D.; Listowski, A.; Wang, X.C. A mini-review on the impacts of climate change on wastewater reclamation and reuse. *Sci. Total Environ.* **2014**, *494–495*, 9–17.
3. Visa, M.; Andronic, L.; Duta, A. Fly ash-TiO₂ nanocomposite material for multi-pollutants wastewater treatment. *J. Environ. Manag.* **2015**, *150*, 336–343.
4. Asghar, A.; Raman, A.A.A.; Daud, W.M.A.W. Advanced oxidation processes for in-situ production of hydrogen peroxide/hydroxyl radical for textile wastewater treatment: A review. *J. Clean Prod.* **2015**, *87*, 826–838.
5. Pang, Y.L.; Abdullah, A.Z. Fe³⁺ doped TiO₂ nanotubes for combined adsorption–sonocatalytic degradation of real textile wastewater. *Appl. Catal. B* **2013**, *129*, 473–481.
6. United States Environmental Protection Agency (EPA). *Guidelines for Water Reuse*; 2012. Available online: <http://nepis.epa.gov/Exe/ZyPURL.cgi?Dockey=P100FS7K.TXT> (accessed on 1 November 2016)
7. De la Cruz, N.; Romero, V.; Dantas, R.F.; Marco, P.; Bayarri, B.; Giménez, J.; Esplugas, S. o-Nitrobenzaldehyde actinometry in the presence of suspended TiO₂ for photocatalytic reactors. *Catal. Today* **2013**, *209*, 209–214.
8. Zhang, Z.; Wu, H.; Yuan, Y.; Fang, Y.; Jin, L. Development of a novel capillary array photocatalytic reactor and application for degradation of azo dye. *Chem. Eng. J.* **2012**, *184*, 9–15.
9. Nakaruk, A.; Ragazzon, D.; Sorrell, C.C. Anatase–rutile transformation through high-temperature annealing of titania films produced by ultrasonic spray pyrolysis. *Thin Solid Films* **2010**, *518*, 3735–3742.
10. Mills, A.; O'Rourke, C.; Moore, K. Powder semiconductor photocatalysis in aqueous solution: An overview of kinetics-based reaction mechanisms. *J. Photochem. Photobiol. A* **2015**, *310*, 66–105.
11. Pelaez, M.; Nolan, N.T.; Pillai, S.C.; Seery, M.K.; Falaras, P.; Kontos, A.G.; Dunlop, P.S.M.; Hamilton, J.W.J.; Byrne, J.A.; O'Shea, K.; et al. A review on the visible light active titanium dioxide photocatalysts for environmental applications. *Appl. Catal. B* **2012**, *125*, 331–349.
12. Zangeneh, H.; Zinatizadeh, A.A.L.; Habibi, M.; Akia, M.; Hasnain Isa, M. Photocatalytic oxidation of organic dyes and pollutants in wastewater using different modified titanium dioxides: A comparative review. *J. Ind. Eng. Chem.* **2015**, *26*, 1–36.
13. Spasiano, D.; Marotta, R.; Malato, S.; Fernandez-Ibanez, P.; Somma, I.D. Solar photocatalysis: Materials, reactors, some commercial, and pre-industrialized applications. A comprehensive approach. *Appl. Catal. B* **2015**, *170–171*, 90–123.
14. Cardoso, J.C.; Lucchiari, N.; Zaroni, M.V.B. Bubble annular photoelectrocatalytic reactor with TiO₂ nanotubes arrays applied in the textile wastewater. *J. Environ. Chem. Eng.* **2015**, *3*, 1177–1184.
15. Kılıç, B.; Gedik, N.; Piravadılı Mucur, S.; Serhan Hergula, A.; Gür, E. Band gap engineering and modifying surface of TiO₂ nanostructures by Fe₂O₃ for enhanced-performance of dye sensitized solar cell. *Mater. Sci. Semicon. Proc.* **2015**, *31*, 363–371.
16. Rico, V.; Romero, P.; Hueso, J.L.; Espinós, J.P.; González-Eliphe, A.R. Wetting angles and photocatalytic activities of illuminated TiO₂ thin films. *Catal. Today* **2009**, *143*, 347–354.
17. Dittrich, Th.; Ofir, A.; Tirosh, S.; Grinis, L.; Zaban, A. Influence of the porosity on diffusion and lifetime in porous TiO₂ layers. *Appl. Phys. Lett.* **2006**, *88*, 182110.
18. Romero-Gómez, P.; Hamad, S.; González, J.C.; Barranco, A.; Espinós, J.P.; Cotrino, J.; González-Eliphe, A.R.

- Band gap narrowing versus formation of electronic states in the gap in N-TiO₂ thin films. *J. Phys. Chem. C* **2010**, *114*, 22546–22557.
19. Romero-Gómez, P.; Rico, V.; Borrás, A.; Barranco, A.; Espinós, J.P.; Cotrino, J.; González-Elipe, A.R. Chemical state of nitrogen and visible surface and Schottky barrier driven photoactivities of N-doped TiO₂ thin films. *J. Phys. Chem. C* **2009**, *113*, 13341–13351.
 20. Bulushev, D.A.; Kiwi-Mínsker, L.; Zaikovskii, V.I.; Lapina, O.B.; Ivanov, A.A.; Reshetnikov, S.I.; Renken, A. Effect of potassium doping on the structural and catalytic properties of V/Ti-oxide in selective toluene oxidation. *Appl. Catal. A* **2000**, *202*, 243–250.
 21. Phanichphant, S.; Nakaruk, A.; Channei, D. Photocatalytic activity of the binary composite CeO₂/SiO₂ for degradation of dye. *Appl. Surf. Sci.* **2016**, *387*, 214–220.
 22. Chong, M.N.; Jin, B.; Chow, C.W.K.; Saint, C. Recent developments in photocatalytic water treatment technology: A review. *Water Res.* **2010**, *44*, 2997–3027.
 23. Liu, S.; Lim, M. Amal, R. TiO₂-coated natural zeolite: Rapid humic acid adsorption and effective photocatalytic regeneration. *Chem. Eng. Sci.* **2014**, *105*, 46–52.
 24. Moustakas, N.G.; Kontos, A.G.; Likodimos, V.; Katsaros, F.; Boukos, N.; Tsoutsou, D.; Dimoulas, A.; Romanos, G.E.; Dionysiou, D.D.; Falaras, P. Inorganic-organic core-shell titania nanoparticles for efficient visible light activated photocatalysis. *Appl. Catal. B* **2013**, *130–131*, 14–24.
 25. Su, T.; Chen, S.; Quan, X.; Zhao, H.; Zhang, Y. A silicon-doped TiO₂ nanotube arrays electrode with enhanced photoelectrocatalytic activity. *Appl. Surf. Sci.* **2008**, *255*, 2167–2172.
 26. Courcot, D.; Grzybowska, B.; Barbaux, Y.; Rigole, M.; Ponchel, A.; Guelton, M. Effect of potassium addition to the TiO₂ support on the structure of V₂O₅/TiO₂ and its catalytic properties in the oxidative dehydrogenation of propane. *J. Chem. Soc. Faraday Trans.* **1996**, *92*, 1609–1617.
 27. Kanakaraju, D.; Kockler, J.; Motti, C.A.; Glass, B.D.; Oelgemoller, M. Titanium dioxide/zeolite integrated photocatalytic adsorbents for the degradation of amoxicillin. *Appl. Catal. B* **2015**, *166–167*, 45–55.
 28. Ghorbani, F.; Younesi, H.; Mehraban, Z.; Celik, M.S.; Ghoreyshi, A.A.; Anbia, M. Preparation and characterization of highly pure silica from sedge as agricultural waste and its utilization in the synthesis of mesoporous silica MCM-41. *J. Taiwan Inst. Chem. Eng.* **2013**, *44*, 821–828.
 29. Chen, Y.D.; Huang, M.J.; Huang, B.; Chen, X.R. Mesoporous activated carbon from inherently potassium-rich pokeweed by in situ self-activation and its use for phenol removal. *J. Anal. Appl. Pyrolysis* **2012**, *98*, 159–165.
 30. Ye, M.; Sun, M.; Liu, Z.; Ni, N.; Chen, Y.; Gu, C.; Kengara, F.O.; Li, H.; Jiang, X. Evaluation of enhanced soil washing process and phytoremediation with maize oil, carboxymethyl- β -cyclodextrin, and vetiver grass for the recovery of organochlorine pesticides and heavy metals from a pesticide factory site. *J. Environ. Manage.* **2014**, *141*, 161–168.
 31. Paillat, L.; Périchet, C.; Pierrat, J.; Lavoine, S.; Filippi, J.; Meierhenrich, U.; Fernandez, X. Purification of vetiver alcohols and esters for quantitative high-performance thin-layer chromatography determination in Haitian vetiver essential oils and vetiver acetates. *J. Chromatogr. A* **2012**, *1241*, 103–111.
 32. Yaseen, M.; Singh, M.; Ram, D. Growth, yield and economics of vetiver (*Vetiveria zizanioides* L. Nash) under intercropping system. *Ind. Crops Prod.* **2014**, *61*, 417–421.
 33. Singh, R.; Narzary, D.; Bhardwaj, J.; Singh, A.K.; Kumar, S.; Kumar, A. Molecular diversity and SSR transferability studies in Vetiver grass (*Vetiveria zizanioides* L. Nash). *Ind. Crops Prod.* **2014**, *53*, 187–198.
 34. Lal, R.K.; Gupta, P.; Gupta, V.; Sarkar, S.; Singh, S. Genetic variability and character associations in vetiver (*Vetiveria zizanioides* L. Nash). *Ind. Crops Prod.* **2013**, *49*, 273–277.
 35. Le, S.T.T.; Yuangpho, N.; Threrujirapapong, T.; Khanitchaidecha, W.; Nakaruk, A. Synthesis of mesoporous materials from vetiver grass for wastewater treatment. *J. Aust. Ceram. Soc.* **2015**, *51*, 40–44.
 36. Rajamanickam, D.; Shanthi, M. Photocatalytic degradation of an azo dye Sunset Yellow under UV-A light using TiO₂/CAC composite catalysts. *Spectrochim. Acta, Part A* **2014**, *128*, 100–108.
 37. Dai, S.; Wu, Y.; Sakai, T.; Du, Z.; Sakai, H.; Abe, M. Preparation of highly crystalline TiO₂ nanostructures by acid-assisted hydrothermal treatment of hexagonal-structured nanocrystalline titania/cetyltrimethylammonium bromide nanoskeleton. *Nanoscale Res. Lett.* **2010**, *5*, 1829–1835.
 38. Bezares, I.; del Campo, A.; Herrasti, P.; Muñoz-Bonilla, A. A simple aqueous electrochemical method to synthesize TiO₂ nanoparticles. *Phys. Chem. Chem. Phys.* **2015**, *17*, 29319–29326.
 39. Hanaor, D.A.H.; Sorrell, C.C. Review of the anatase to rutile phase transformation. *J. Mater. Sci.* **2011**, *46*, 855–874.

40. Lin, C.P.; Chen, H.; Nakaruk, A.; Koshy, P.; Sorrell, C.C. Effect of annealing temperature on the photocatalytic activity of TiO₂ thin films. *Energy Procedia* **2013**, *34*, 627–636.
41. Shannon, R.D. Revised effective ionic radii and systematic studies of interatomic distances in halides and chalcogenides. *Acta Crystallogr. A* **1976**, *32*, 751–767.
42. Chen, W.F.; Koshy, P.; Huang, Y.; Adabifiroozjaei, E.; Yao, Y.; Sorrell, C.C. Effects of precipitation, liquid formation, and intervalence charge transfer on the properties and photocatalytic performance of cobalt- or vanadium-doped TiO₂ thin films. *Int. J. Hydrogen Energy* **2016**, *41*, 19025–19056.
43. Nakaruk, A.; Lin, C.Y.W.; Koshy, P.; Sorrell, C.C. Iron doped titania thin films prepared by spin coating. *Adv. Appl. Ceram.* **2012**, *111*, 129–133.
44. Lin, Z.; Orlov, A.; Lambert, R.M.; Payne, M.C. New insights into the origin of visible light photocatalytic activity of nitrogen-doped and oxygen-deficient anatase TiO₂. *J. Phys. Chem. B* **2005**, *109*, 20948–20952.
45. Prasai, B.; Cai, B.; Underwood, M.K.; Lewis, J.P.; Drabold, D.A. Properties of amorphous and crystalline titanium dioxide from first principles. *J. Mater. Sci.* **2012**, *47*, 7515–7521.
46. Yu, J.G.; Yu, H.G.; Cheng, B.; Zhao, X.J.; Yu, J.C.; Ho, W.K. The effect of calcination temperature on the surface microstructure and photocatalytic activity of TiO₂ thin films prepared by liquid phase deposition. *J. Phys. Chem. B* **2003**, *107*, 13871–13879.
47. Zhang, F.; Maeda, K.; Takata, T.; Domen, K. Improvement of the photocatalytic hydrogen evolution activity of Sm₂Ti₂S₂O₅ under visible light by metal ion additives. *J. Catal.* **2011**, *280*, 1–7.
48. Tian, F.; Wu, Z.; Chen, Q.; Yan, Y.; Cravotto, G.; Wu, Z. Microwave-induced crystallization of AC/TiO₂ for improving the performance of rhodamine B dye degradation. *Appl. Surf. Sci.* **2015**, *351*, 104–112.
49. Pesci, F.M.; Wang, G.; Klug, D.R.; Li, Y.; Cowan, A.J. Efficient suppression of electron–hole recombination in oxygen-deficient hydrogen-treated TiO₂ nanowires for photoelectrochemical water splitting. *J. Phys. Chem. C* **2013**, *117*, 25837–25844.
50. Wang, G.; Wang, H.; Ling, Y.; Tang, Y.; Yang, X.; Fitzmorris, R.C.; Wang, C.; Zhang, J.Z.; Li, Y. Hydrogen-treated TiO₂ nanowire arrays for photoelectrochemical water splitting. *Nano Lett.* **2011**, *11*, 3026–3033.
51. Zhang, J.; Zhao, Z.; Wang, X.; Yu, T.; Guan, J.; Yu, Z.; Li, Z.; Zou, Z. Increasing the oxygen vacancy density on the TiO₂ surface by La-doping for dye-sensitized solar cells. *J. Phys. Chem. C* **2010**, *114*, 18396–18400.
52. Fujii, K.; Sato, Y.; Takase, S.; Shimizu, Y. Effects of oxygen vacancies and reaction conditions on oxygen reduction reaction on Pyrochlore-Type lead-ruthenium oxide. *J. Electrochem. Soc.* **2015**, *162*, F129–F135.
53. Xu, L.; Jiang, Q.; Xiao, Z.; Li, X.; Huo, J.; Wang, S.; Dai, L. Plasma-engraved Co₃O₄ nanosheets with oxygen vacancies and high surface area for the oxygen evolution reaction. *Angew. Chem. Int. Ed.* **2016**, *55*, 5277–5281.
54. Huang, S.H.; Wang, C.C.; Liao, S.Y.; Gan, J.Y.; Perng, T.P. CNT/TiO₂ core–shell structures prepared by atomic layer deposition and characterization of their photocatalytic properties. *Thin Solid Films* **2016**, *616*, 151–159.
55. Zhang, G.; Teng, F.; Zhao, C.; Chen, L.; Zhang, P.; Wang, Y.; Gong, C.; Zhang, Z.; Xie, E. Enhanced photocatalytic activity of TiO₂/carbon@TiO₂ core–shell nanocomposite prepared by two-step hydrothermal method. *Appl. Surf. Sci.* **2014**, *311*, 384–390.
56. Lee, J.M.; Han, S.B.; Kim, J.Y.; Lee, Y.W.; Ko, A.R.; Roh, B.; Hwang, I.; Park, K.W. TiO₂@carbon core–shell nanostructure supports for platinum and their use for methanol electrooxidation. *Carbon* **2010**, *48*, 2290–2296.

